Electrochimica Acta 365 (2021) 137349

Contents lists available at ScienceDirect

Electrochimica Acta

journal homepage: www.elsevier.com/locate/electacta

Optimization of high potential cathode materials and lithium conducting hybrid solid electrolyte for high-voltage all-solid-state batteries

Hakgyoon Yu[a], Jong Su Han[a], Gil Chan Hwang[b,*], Jung Sang Cho[c], Dong-Won Kang[d,*], Jae-Kwang Kim[a,*]

[a] Department of Energy Convergence Engineering, Cheongju University, Cheongju, Chungbuk 28503, Republic of Korea
[b] Department of Earth System Sciences, Yonsei University, Seoul 03722, Republic of Korea
[c] Department of Engineering Chemistry, Chungbuk National University, Chungbuk 28644, Republic of Korea
[d] School of Energy Systems Engineering, Chung-Ang University, Seoul 06974, Republic of Korea

ARTICLE INFO

Article history:
Received 20 August 2020
Revised 10 October 2020
Accepted 21 October 2020
Available online 25 October 2020

Keywords:
$LiMn_{0.8}Fe_{0.2}PO_4$
Crystal structure
Scavenging effect
High voltage
All-solid-state battery

ABSTRACT

$LiMn_{0.8}Fe_{0.2}PO_4$ (LMFP) as high potential cathode is synthesized by a modified mechanical activation method and tested for use in all-solid-state high-voltage rechargeable lithium ion batteries. The influence of synthesis condition on the atomic structure, particle size, morphology, surface area, and electrochemical performance of the active material is investigated. A high dielectric constant ceramic (Al_2O_3) is composited in $Li_{1.3}Al_{0.3}Ge_{1.7}P_3O_{12}$ (LAGP)-based lithium conducting hybrid solid electrolyte, and a higher lithium ion transference number is observed owing to the anion scavenging effect of Al_2O_3. An all-solid-state LMFP battery is constructed with a graphite anode and the hybrid solid electrolyte. At current densities of 0.1, 1, 3, and 10 C, initial discharge capacities of 156.3, 133.7, 111.8, and 71.4 mAh g^{-1} (91.9, 78.6, 65.8, and 42% of theoretical capacity) are obtained with low corresponding capacity fade of 0.001, 0.02, 0.01, and 0.013% per cycle evaluated over 300 cycles, even after charging to 4.5 V.

1. Introduction

Lithium metal phosphate ($LiMPO_4$, M = Co, Fe, Mn) is a stable and promising cathode material for lithium batteries with many advantages, including low cost, environmental compatibility, a long cycle life, and a relatively high capacity (170 mAh g^{-1}) [1-22]. However, $LiMPO_4$ has lower capacity and energy density than conventional lithium metal oxide ($LiMO_2$, M = Co, Ni, Mn). One approach to exploiting the inherently high capacity and high energy density of $LiMPO_4$ is to use mixed olivine phosphates with the general formula $LiMn_yFe_{1-y}PO_4$, where the proportion of Mn can be adjusted to tailor promising candidate materials with operating cell voltages of 3.4–4.1 V vs. Li^+/Li [4,23,24]. This is providential, because the upper end of this range is not so high that the organic electrolyte decomposes, and the lower bound is not so low that power density is sacrificed. The amount of Mn in $LiMn_yFe_{1-y}PO_4$ is crucial, because a cathode material that contains too much Mn exhibits poor cycling stability. Ma et al. fabricated $LiMn_yFe_{1-y}PO_4$ thin films using a modified electrostatic spray deposition and sol–gel technique. An electrode consisting of a thin film of $LiMn_{0.4}Fe_{0.6}PO_4$ yielded better electrochemical performance than electrodes made of pure $LiFePO_4$ or $LiMnPO_4$ [25]. Moreover, a previous study in which the electrochemical performances of $LiMn_yFe_{1-y}PO_4$ (y = 0–1) materials were compared showed that $LiMn_{0.4}Fe_{0.6}PO_4$ had a high energy density and exhibited the best electrochemical properties [4]. Reducing the $LiMn_yFe_{1-y}PO_4$ particle size was also beneficial for electrode conductivity. Heating temperature is also a key factor in optimizing particle size in $LiMn_yFe_{1-y}PO_4$ (y = 0–1) materials [26-29].

All-solid-state lithium batteries having the advantages of high thermal and electrochemical stability have recently attracted a great deal of attention from many research groups [30,31]. Although studies of all-solid-state lithium batteries have focused mainly on improving the solid electrolyte, the choice of cathode material is also important for achieving high energy density at high operating voltages. The commercially available electrode material $LiNi_{1-2x}Co_xMn_xO_2$ (NCM) has a layered structure that undergoes an unstable crystal transition at high voltages (>4.2 V). This is a drawback, because it results in rapid capacity degradation with cycling [32,33]. The $LiMn_yFe_{1-y}PO_4$ cathode may be suitable for

* Corresponding authors.
E-mail addresses: gchwang@yonsei.ac.kr (G.C. Hwang), kangdwn@cau.ac.kr (D.-W. Kang), aekwang@cju.ac.kr (J.-K. Kim).

https://doi.org/10.1016/j.electacta.2020.137349
0013-4686/

all-solid-state lithium batteries operated at high voltages, because it has a stable crystal structure with covalent bonds between oxygen and phosphorus.

Another issue associated with the high voltage lithium ion battery is the electrochemical stability of the electrolytes. Although carbonate-based liquid electrolytes possess high ionic conductivity, they are not suitable for high voltage lithium ion batteries owing to their low oxidation voltage and flammability [34-36]. Therefore, ceramic solid electrolytes have attracted significant attention for the improvement of the safety and energy density with high voltage operation. Ceramic solid electrolytes are largely divided into two classes: sulfide- and oxide-based. However, the interfacial resistance between ceramic solid electrolytes and electrodes is high, and therefore, a hybrid solid electrolyte, composited with a small amount of liquid electrolyte, was proposed to address the aforementioned problem. Oxide-based ceramic solid electrolytes are preferable for the preparation of hybrid solid electrolytes because they are more stable in moist atmosphere as compared to the sulfide ceramic solid electrolytes. Among the oxide-based ceramic solid electrolytes, NASICON structures such as ($Li_{1+x}Al_xX_{2-x}P_3O_{12}$, X= Ti, Ge) have shown high ionic conductivity and high atmospheric stability [35,36]. The addition of a liquid electrolyte as an additive in the NASICON-type oxide ceramic-based hybrid solid electrolyte can reduce the interfacial resistance; however, the lithium ion transference number decreases owing to the ion aggregation of Li^+ with anions. High dielectric constant and Lewis acidity of ceramics such as Al_2O_3, TiO_2, and $BaTiO_3$ are effective in suppressing ion aggregation and improving the lithium ion transference number [37].

For this study, we chose a y value of 0.8 and applied a modified mechanical activation method to prepare uniformly carbon-coated $LiMn_{0.8}Fe_{0.2}PO_4$ for use in a high voltage all-solid-state lithium battery. Al_2O_3 was added to a $Li_{1.3}Al_{0.3}Ge_{1.7}P_3O_{12}$ (LAGP)-based hybrid solid electrolyte to enhance the lithium ion transference number. Previously, favorable electrochemical properties could not be obtained in $LiMn_{0.8}Fe_{0.2}PO_4$ cells due to the decomposition of organic electrolyte at high voltages. However, when the hybrid solid electrolyte is applied in the cells, high voltage operation is possible and electrochemical characteristics can be consequently improved. The primary objectives of this study were to optimize the process of synthesis and investigate changes in $LiMn_{0.8}Fe_{0.2}PO_4$ and hybrid solid electrolyte properties induced by the calcination temperature and the addition of a high dielectric constant ceramic in order to realize a high-performance all-solid-state lithium ion battery.

2. Experimental

2.1. Synthesis of $LiMn_{0.8}Fe_{0.2}PO_4$

$LiMn_{0.8}Fe_{0.2}PO_4$ (LMFP) composites were prepared by a modified mechanical activation method using acetylene black powder as a carbon source. The method involved rotary evaporation, high-energy ball milling, and firing steps [28]. Previously optimized synthetic conditions (ball milling time) were employed to prepare $LiMn_{0.8}Fe_{0.2}PO_4$ in this study [27]. Acetylene black (≥99.9 wt%) was purchased from Alfa Aesar. All other chemicals (99%) were obtained from Aldrich. Stoichiometric quantities of Li_2CO_3, $FeC_2O_4{\bullet}2H_2O$, $Mn(COOCH_3)_2{\bullet}4H_2O$, and $NH_4H_2PO_4$, and 5.0 wt% acetylene black were stirred with 60 wt% triply distilled water at room temperature for 7 h. Solid powder was obtained from the homogeneous mixture by rotary evaporation at 80 °C for 2 h at 60 rpm. The solid powder was ball-milled for 15 h at room temperature under an argon atmosphere in a hardened steel vial with zirconia balls at a ball-to-powder weight ratio of 10:3 using a SPEX mill at 1000 rpm. The milled powder formed pellets when calcined at temperatures ranging from 500 to 700 °C for 10 h in a nitrogen atmosphere. For the sake of simplicity and to highlight the firing temperature, the samples were designated LMF5 (500 °C), LMF6 (600 °C), and LMF7 (700 °C).

2.2. Preparation of quasi-hybrid solid electrolyte

Hybrid solid electrolyte (HSE) was prepared using a phase inversion process [38,39]. For the hybrid solid electrolyte, $Li_{1.3}Al_{0.3}Ge_{1.7}P_3O_{12}$ (LAGP) synthesized via a solid-state reaction was mixed with PVdF-TrFE [poly(vinylidene fluoride-trifluoroethylene)] and Al_2O_3 (size: 50 nm, dielectric constant: 8.6, from Aldrich) in acetone: *N*-methyl pyrrolidone (NMP) (6:4 vol.%) solvent. The ceramic-polymer hybrid film was prepared and subsequently dried to remove the solvent. The hybrid film was then soaked in liquid electrolyte (1 M $LiPF_6$ in EC/DMC) and the resulting hybrid solid electrolyte contained 10 wt% liquid electrolyte as an additive.

2.3. Characterization

The chemical composition of the material was determined by inductively coupled plasma optical emission spectroscopy (ICP-OES) on an Optima 4300 DV spectrometer (PerkinElmer Inc., Waltham, MA). Carbon content was determined with a CHNS 932 elemental analyzer (LECO, St. Joseph, MI). X-ray powder diffraction (XRD) analysis and Rietveld refinement, used for crystallographic structural characterization, was performed on a D5005 series diffractometer (Siemens, Munich) equipped with a Cu $K\alpha$ radiation source (35 mA/40 kV) and a graphite monochromator. Data for Rietveld structural refinement were collected from 15° to 120° (2θ) with a 0.02° step interval and a step time of 10 s. The sample was rotated at 30 rpm during data collection to minimize any preferred orientation effects and statistical errors in the calculations. The crystal structure was assigned to the *Pnma* space group and refined with the FullProf program (CCP14) [40]. Scanning electron microscopy (SEM) imaging was performed with a XL 30 FEG SEM (Philips, Amsterdam). The morphology and thickness of the carbon coating were examined with high-resolution (HR) transmission electron microscopy with a JEM 3010 HR-TEM (JEOL, Tokyo). The specific surface area was determined by the Brunauer-Emmett-Teller (BET) method with N_2 sorption data collected on an ASAP 2020 Analyzer (Micromeritics, Norcross, GA). Thermogravimetric analysis (TGA) of all materials was performed on an SDT Q600 analyzer (TA Instruments, New Castle, DE) under flowing oxygen or nitrogen at a heating rate of 5 °C min^{-1}.

2.4. Evaluation of electrochemical properties

To prepare the cathode, the $LiMn_{0.8}Fe_{0.2}PO_4$ active material, carbon black, and poly(vinylidene fluoride) binder (PVdF, Aldrich) were mixed in a 92:4:4 ratio by weight and made into a viscous slurry in NMP. The slurry was cast onto aluminum foil and dried at 95 °C under vacuum for 12 h. The film was cut into 0.95 cm^2 circular discs that weighed ~4.0 mg each for use as cathode material. The coin-type Li/LMFP half-cell was fabricated by stacking a 300-μm thick lithium metal anode (Cyprus Foote Mineral Co.) and a LMFP-based cathode with Celgard@ 2200 separator film or a hybrid solid electrolyte (HSE). For comparison, 1 M $LiPF_6$ in 1:1 (v/v) ethylene carbonate (EC):dimethyl carbonate (DMC) was used as a liquid electrolyte. Electrochemical performance tests were carried out from 2.5 to 4.5 V at room temperature using an automatic galvanostatic charge–discharge unit and a WBCS3000 battery cycler (WonATech, Seoul). The experiments were performed at different current density rates ranging from 0.1 C (0.069 mA cm^{-2}) to 10 C (6.9 mA cm^{-2}) for a 3 cm × 7 cm pouch-type all-solid-state C/HSE/LMFP full cell. To prepare a pouch-type full solid-state

Table 1
Unit cell parameters of LMFP determined by Rietveld structural refinement.

Sample No.	LMF5	LMF6	LMF7
a (Å)	10.3804(2)	10.3837(3)	10.3814(5)
b (Å)	6.0451(1)	6.0477(2)	6.0459(3)
c (Å)	4.71412(8)	4.7167(1)	4.7182(2)
V (Å^3)	295.816(9)	296.20(1)	296.14(2)

battery, the LMFP cathode film is stacked onto a piece of graphite anode sticking on a pouch film and separated by a hybrid solid electrolyte before soldering and sealing of the pouch cell.

3. Results and discussion

The chemical composition of the samples determined by ICP-OES analysis had a theoretical Li:Mn:Fe:P molar ratio of 1.01:0.81:0.19:0.99 (±0.01). Elemental analysis indicated the $LiMn_{0.8}Fe_{0.2}PO_4$ material contained ~6 wt% carbon. The LMFP XRD patterns obtained from the Rietveld refinements are shown in Fig. 1. The data were in very good agreement and confirmed the as-prepared LMFP had an olivine structure in space group *Pnma*. The unit cell parameters determined by Rietveld refinement are listed in Table 1 (Table S1). No peaks due to impurities were observed in any of the patterns, and the peak profiles were quite narrow, which indicated a well-crystallized phase. The lines at the bottom of Fig. 1 mark the calculated positions of the allowed reflections. The narrow-excluded regions were due to contributions from the cryostat. The reliability factor (R_{wp}) of each sample was ~10, which suggested a good solution. All LMFP lattice parameters were greater than those of $LiFePO_4$ [41]. The cell volume based on the unit cell parameters *a* and *b* was largest in LMF6 obtained at 600 °C, but magnitude of *c* increased with increasing calcination temperature. The olivine composite synthesized at 500 °C had a denser structure. The transport of lithium ion in the LMFP crystal occurred along the *b*-direction, so the short path length in LMF5 was beneficial for fast ion diffusion.

$LiMn_{0.8}Fe_{0.2}PO_4$ in the olivine structure exhibited a hexagonal close-packed arrangement of oxygen and Li, while Mn/Fe ions were located in half of the octahedral sites. P atoms occupied one out of eight tetrahedral positions. One Mn/FeO_6 octahedron shared common edges with two LiO_6 octahedra. Each PO_4 group shared one common edge with a Fe/Mn-O_6 octahedron and two with LiO_6 octahedra. The Mn/Fe-O_6 octahedra shared four corners in the *cb*-plane and were crosslinked along the *a*-axis by the PO_4 groups to form a three-dimensional network (Fig. 2). The Li ions were located in rows of edge-shared Li–O_6 octahedra running along the *a*-axis, which appeared between two consecutive Mn/Fe–O_6 layers lying on the *cb*-plane [42,43].

Mn/Fe–O_6 octahedra had two axial oxygen atoms (O1, O2) and four equatorial oxygen atoms (O3, O3). The six Mn/Fe–O bonds were categorized as 1(O1) *a* + 1(O2) *a* and 4(O3) *e* (Fig. 3). The electron interactions in the lattice distorted the Mn/Fe–O_6 octahedra, as the O1–Mn/Fe–O2 bond angle deviated from 180° The O3–Mn/Fe–O3 angles along the equatorial plane perpendicular to the O1–Mn/Fe–O2 line were larger and smaller than the expected 90°, causing distortion that formed a pair of scissors[42]. The differences in all three axes in the samples were a measure of the high degree of distortion and anisotropy induced by the calcination temperature, as maximum scissoring was observed in LMF5. One equatorial bond was the smallest observed (64.85°), while the other large (118.74°). The difference between the angles in LMF7 was smallest among the samples. The geometry of the Mn/Fe–O_6 octahedra in LMF7 was unusual, as the length of the O3–Mn/Fe–O3 bonds that formed the larger angle was smaller by 0.01–0.02 Å, while

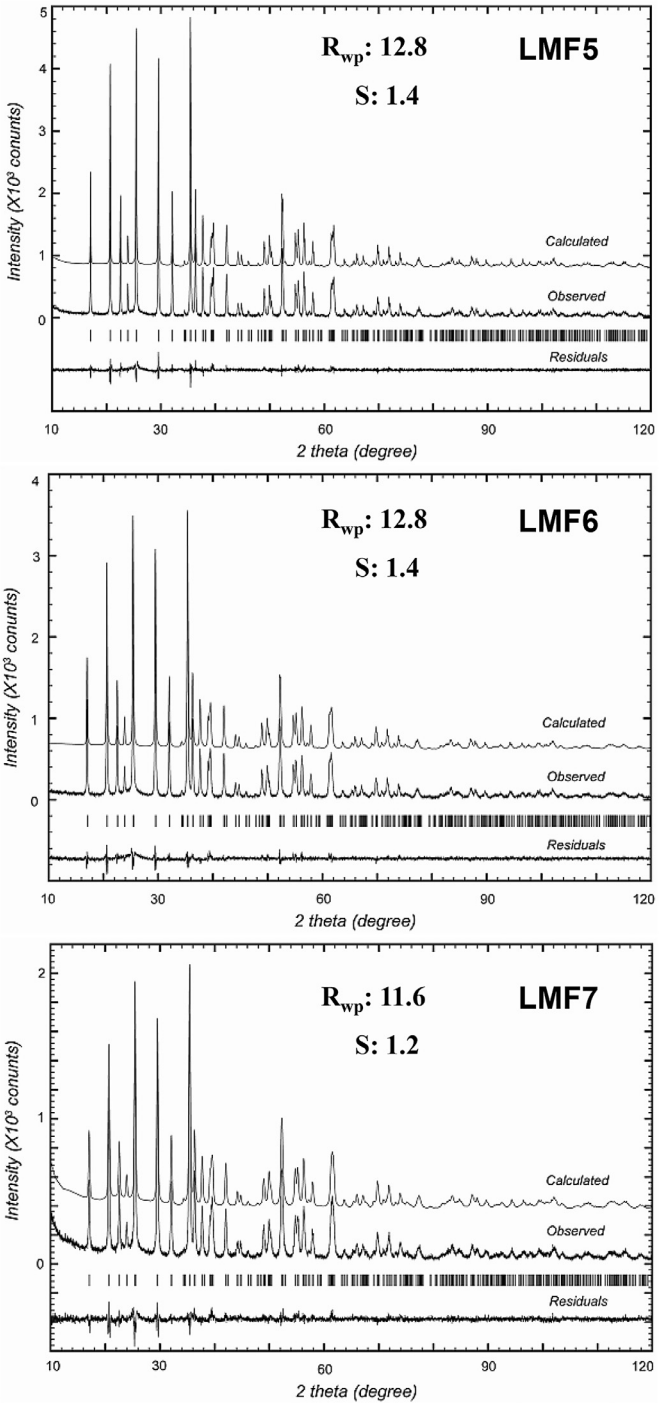

Fig. 1. X-ray diffraction profiles from the Rietveld refinements for LMF5, LMF6 and LMF7.

the other two bonds were longer by 0.01–0.02 Å. However, the sum of the bond lengths of the O3–Mn/Fe bond of the larger angle and the Mn/Fe–O3 bond of the smaller angle remained 4.36 Å in all samples. The length of the axial Mn/Fe–O1 bond in LMF7 was the shortest among the samples, but the Mn/Fe–O2 bond length in LMF5 was shortest by 0.02–0.03 Å. Hence, Mn/Fe–O1 coherence in LMF7 was strongest among the samples, while Mn/Fe–O2 coherence in LMF5 was stronger than in the other samples.

Calculations from SEM and BET analysis showed that the average particle size increased significantly with increasing synthesis temperatures from 500 °C to 700 °C. The SEM images are

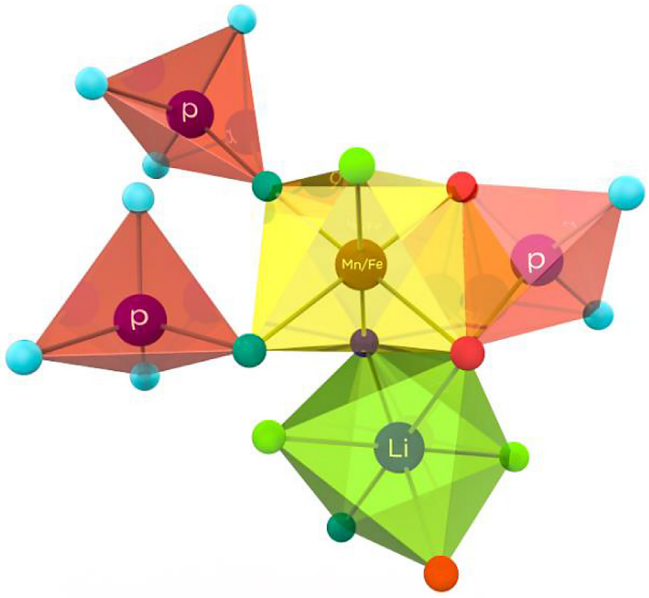

Fig. 2. Local networking geometry of Mn/Fe–O_6 and Li–O_6 octahedra and PO_4 tetrahedra in $LiMn_{0.8}Fe_{0.2}PO_4$.

shown in Fig. 4, and Table S2 lists the particle properties of the $LiMn_{0.8}Fe_{0.2}PO_4$ samples according to calcination temperature. It can be seen in Fig. 4 that the average particle size increased with increasing temperature, while the most uniform size distribution was achieved at 500 °C. Based on the BET surface area measurements, LMF5 had the largest surface area of all the samples. LMF7 and LMF6 differed in BET surface area and pore volume, but their pore sizes were nearly equal. The ratio of the surface area of each sample to that of LMF7 decreased from 1.43 (LMF5) to 1.41 (LMF6) to 1 (LMF7), while the ratio of average pore volume decreased from 1.64 (LMF5) to 1.42 (LMF6) to 1 (LMF7). Thus, the average pore volumes and surface areas of the composite particles largely depended on the calcination temperature, as LMF5 had the largest surface area and largest average pore volume and exhibited more uniform morphology. Larger surface area and pore volume increased the effective area of overlap between the electrode materials and the electrolyte, thereby improving ion transferability. The TG/DTA curves of the LMF5 sample obtained in (a) air and (b) nitrogen atmosphere are displayed in Fig. S1. In the range between room temperature and 200 °C, some weight loss was seen in both TG curves that corresponded to the elimination of water. In air, the weight of LMF5 increased at 350 °C; however, no weight increase occurred under nitrogen. Air causes a relative weight gain with the complete oxidation of iron metal to the ferric state. Metal oxidation occurs primarily in Fe^{2+} sites, because Mn^{2+} is more stable than Mn^{3+} in an oxygen atmosphere [44]. Rapid weight loss was observed in carbon-coated LMF5 in air around 500 °C due to the decomposition of carbon. The carbon content in synthesized LMF5 was approximately 8.0% based on weight lost during TGA. The carbon content of LMF5 matched the value determined by elemental analysis. From the TG curves obtained under nitrogen, we were able to conclude that the carbon coating did not de-

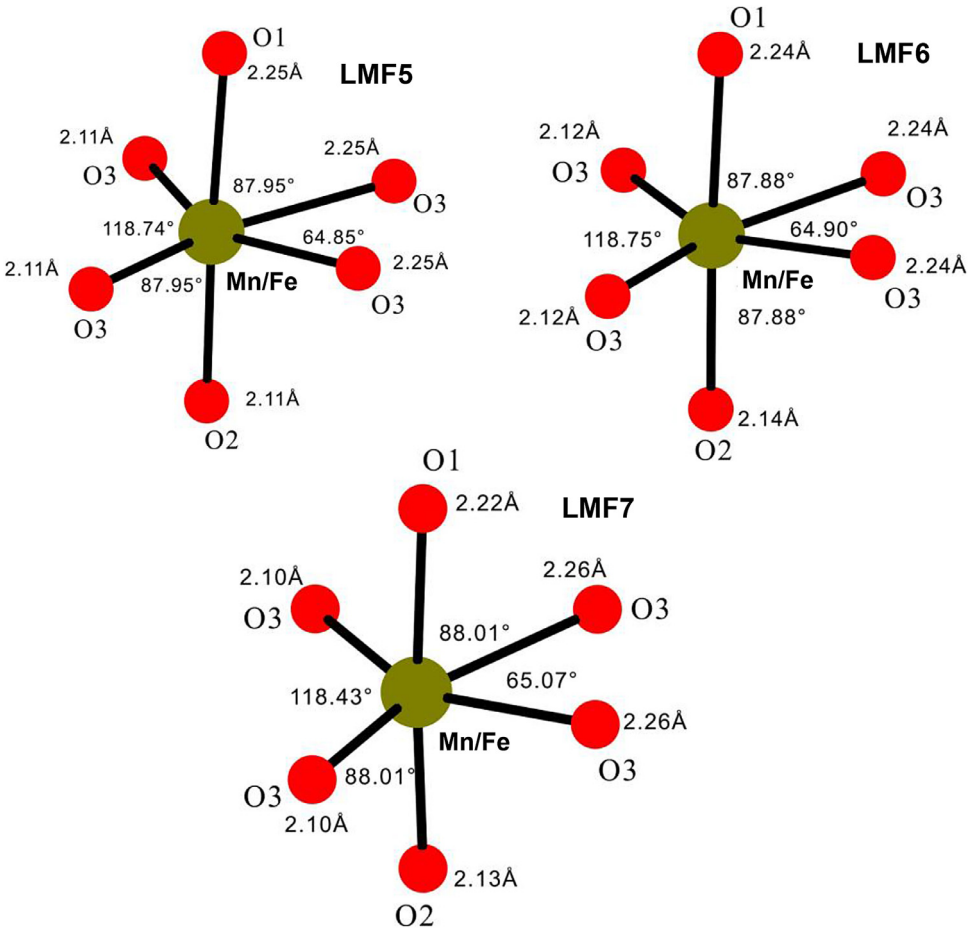

Fig. 3. Distances and angles of Mn/Fe–O bonds in the Mn/Fe–O_6 octahedral geometry of $LiMn_{0.8}Fe_{0.2}PO_4$.

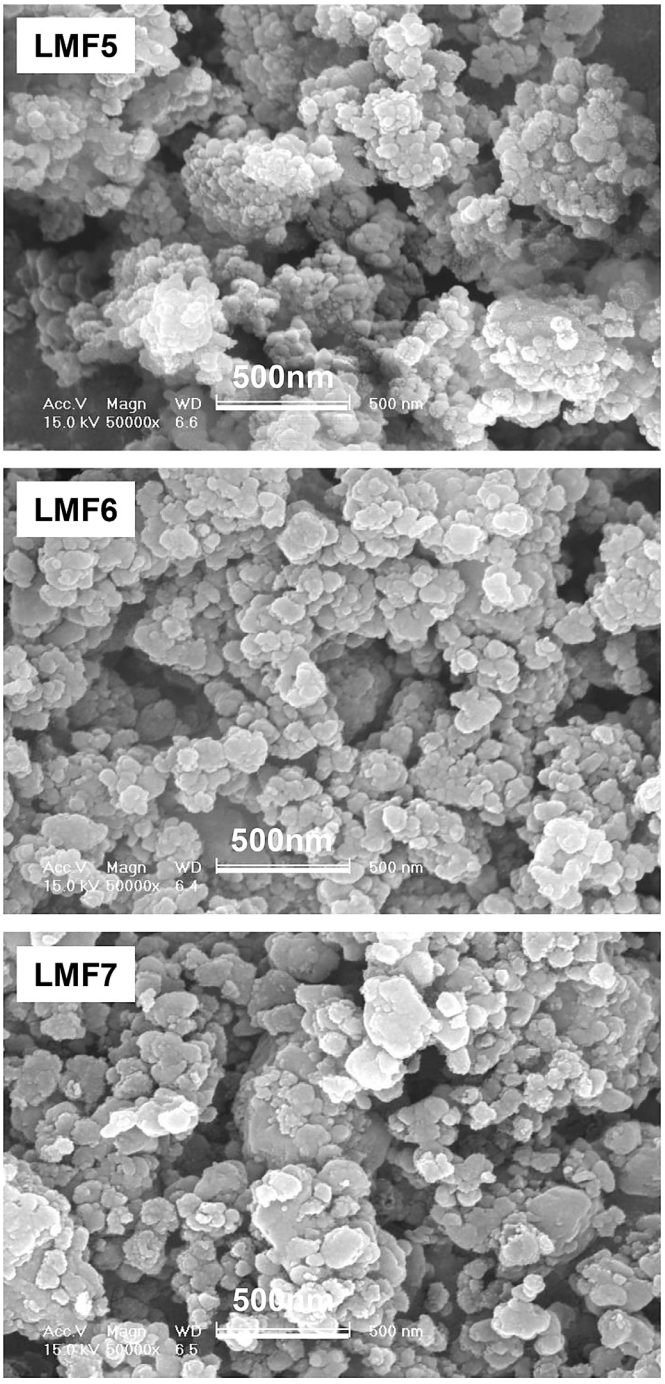

Fig. 4. SEM images of LMF5, LMF6, and LMF7 at different calcination temperatures.

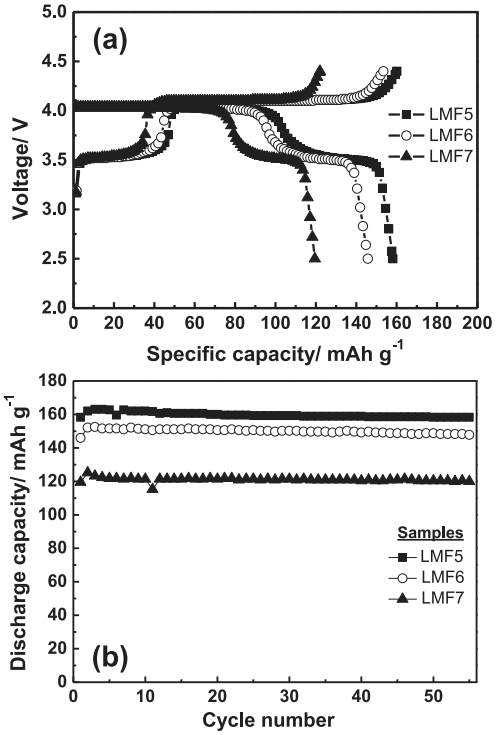

Fig. 5. Initial charge–discharge curves (a) and cycle behaviors (b) of $Li/LiMn_{0.8}Fe_{0.2}PO_4$ cells according to synthetic temperature.

compose, and the LMFP cathode material was stable up to 850 °C. The performance of LMF5 in electrochemical tests was better than that of the other two samples. The LMF5 delivered higher charge and discharge capacities when tested at a current density of 0.1 C (0.069 mA cm^{-2}) (Fig. 5a). The initial charge capacities of LMF5, LMF6, and LMF7 were 160, 153, and 122 mAh g^{-1}, respectively. The discharge capacities of LMF5, LMF6, and LMF7 were 158, 146, and 119 mAh g^{-1}, respectively. Thus, LMF5 exhibited better performance with a high active material utilization of 92.7% during discharge. When compared to LMF6, the difference of initial discharge capacity was about 10 mAh g^{-1}, but the difference in capacity was around 30 mAh g^{-1} when comparing LMF6 and LMF7. Thus, when calcination temperature was increased from 600 °C to 700 °C, the character of material changed significantly. These results were consistent with our SEM observations. The discharge capacities of the materials on cycling are shown in Fig. 5b. The discharge capacities of all samples gradually increased with the number of cycles. A possible reason for the gradual increase in discharge capacity was the formation of fissures in the carbon layers as the number of cycles increased. These fissures facilitated penetration of the electrolyte into the particles [45]. The LMF5 exhibited nearly stable performance up to cycle 55, with a minor increase in capacity from an initial value of 158 mAh g^{-1} to 163 mAh g^{-1}, after which it remained stable. The discharge capacities of LMF6 and LMF7 were 146 and 119 mAh g^{-1}, respectively. These values were not only lower than those observed with LMF5, but they also indicated lower discharge capacities after 55 cycles. The charge-discharge efficiency and stability were better in LMF5.

An all-solid-state LMFP battery was fabricated with $Li_{1.3}Al_{0.3}Ge_{1.7}P_3O_{12}$ (LAGP) lithium-conducting ceramic synthesized by a solid-state reaction. The resulting LAGP powder (75 wt%) was then composited with PVdF-TrFE [poly(vinylidene fluoride-trifluoroethylene)] (10 wt%), Al_2O_3 (5 wt%) and a liquid electrolyte (10 wt%) [46,47]. The hybrid solid electrolyte (HSE) had a flexible film form (Fig. 6a) with a homogeneously distributed polymer and conducting ceramic (Fig. 6b). Although the composited liquid electrolyte occupied the ceramic-ceramic and polymer-ceramic boundaries, the HSE appeared as a solid film. Notably, Al_2O_3 as a high dielectric constant and Lewis acidity ceramic plays the role of a scavenger to trap (PF_6^-) anions, thereby allowing a high ionic conductivity of 4.5×10^{-3} S cm^{-1} at 30 °C (Fig. 6c). Moreover, the HSE had a high oxidation voltage (>5.0 V), which enables charging at high voltages (Fig. S2) and high thermal stability to 465 °C (Fig. S3).

Raman spectra of the HSE containing a liquid electrolyte additive (1 M $LiFP_6$ salt in EC/DMC) were measured over the frequency range of 0–3500 cm^{-1}. Raman spectroscopy is advantageous for investigating Li^+ - PF_6^- pairs, especially in the range 730–750 cm^{-1};

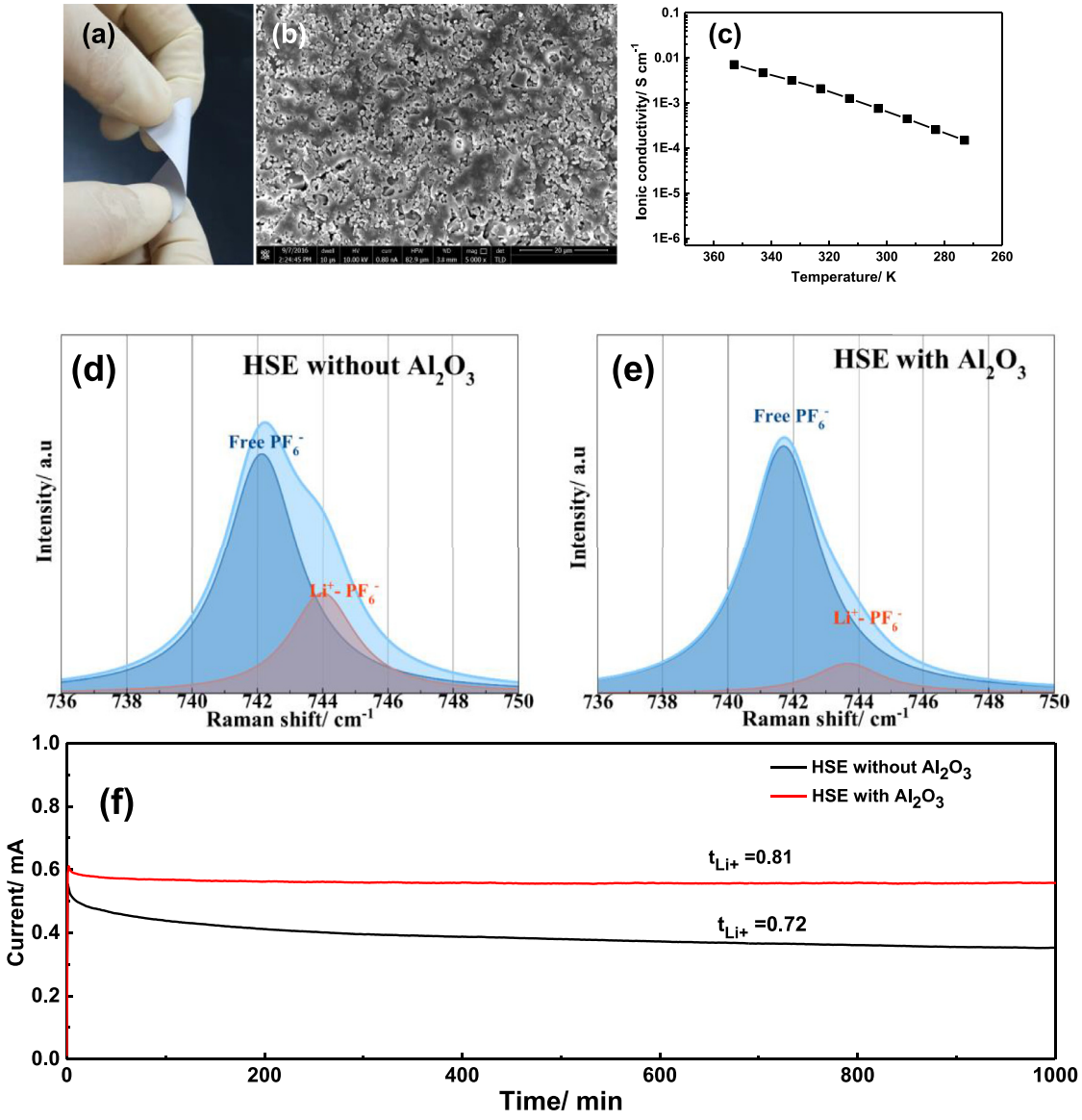

Fig. 6. (a) Photograph, (b) SEM image, and (c) ionic conductivity of the hybrid solid electrolyte (HSE+Al_2O_3). Deconvoluted Raman bands (d, e) of PF_6^- anion in the region 736–750 cm^{-1} and (f) Chronoamperometry results for HSE without Al_2O_3 and HSE with Al_2O_3.

this is because the strong mode, corresponding to the contraction-expansion of the entire PF_6^- ion stretching the vibrational mode of PF_6 observed at ~742 cm^{-1}, is sensitive to interactions (Li^+ - PF_6^-) [48]. The solid lines depicted in Fig. 6(d, e) denote the results of the experimental spectra bandfit, using Lorentzian profiles. Two peaks are observed in the spectra of HSE containing 10 wt% liquid electrolyte: first, at ~742 cm^{-1}, which is due to the symmetric stretching vibration of free PF_6^- anions, and second, at ~744 cm^{-1}, which is due to Li^+ - PF_6^- ion pairs. With the addition of the high dielectric constant Al_2O_3 ceramic, the ion pair signal is significantly decreased. The ion pairing in HSE decreased by the scavenging of anions of the liquid electrolyte additive, thereby increasing the lithium transference number. The lithium transference number (t_{Li+}) was measured using chronoamperometry following the Bruce-Vincent method, as shown in Fig. 6f. The calculated t_{Li+} obtained by comparing the maximum and equilibrium current values are 0.72 and 0.81 for the HSE without Al_2O_3 (LAGP 80 wt%, PVdF-TrFE 10 wt% and liquid electrolyte 10 wt%) and HSE with Al_2O_3, respectively. In comparison, the lithium ion conductivity for both types of HSE is considerably larger than that for the conventional liquid electrolyte, ~0.4 [49]. This may be because of the contributions from the lithium conducting LAGP solid electrolyte. Moreover, the addition of Al_2O_3 increased the lithium ion conductivity in the HSE because the high dielectric constant ceramic traps the anion (PF_6^-), thereby promoting the movement of free lithium ions. This experimental evidence confirms the contribution of Al_2O_3 in the HSE to the ion transport mechanism.

The all-solid-state battery prepared with a LMF5 cathode, graphite anode, and HSE (containing Al_2O_3) performed satisfactorily at 25 °C, even at higher current densities (Fig. S4). The initial charge-discharge properties of the LMF5 solid battery at higher current densities of 0.1, 1, 3, and 10 C, corresponding to 0.063, 0.63, 1.89, and 6.3 mA cm^{-2}, are shown in Fig. 7a. The initial charge capacities were 158.1, 135.2, 113.9, and 81.5 mAh g^{-1}, and the discharge capacities were 156.3, 133.7, 118.8, and 71.4 mAh g^{-1}. The ΔV between the average charge and discharge potentials of Fe^{2+}/Fe^{3+} and Mn^{2+}/Mn^{3+}, which corresponded to the mid-points of the curves, increased with current density. At the low discharge

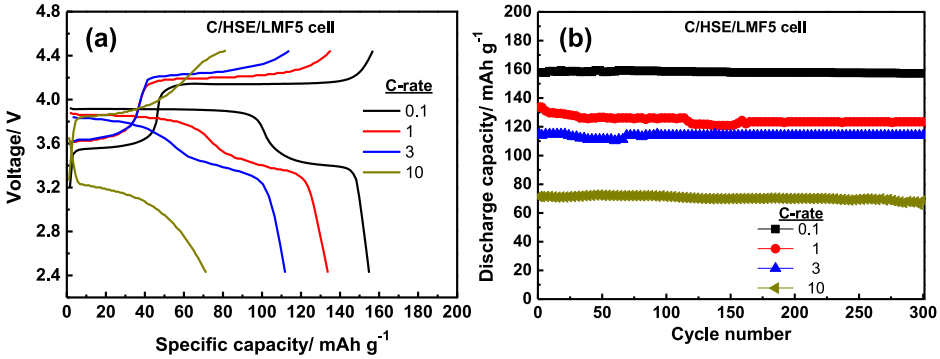

Fig. 7. (a) Initial charge–discharge curves and (b) cycle performances of C/HSE+Al_2O_3/LMF5 all-solid-state lithium batteries at 0.1, 1, 3 and 10 C-rates.

rate of 1 C, the cells performed exceedingly well with high active material utilization (>83%). A reasonable active material utilization of >42% was attained at the high 10 C-rate as well. This excellent performance at high current density is not observed with all-solid-state batteries. From the profile, we concluded that the redox reaction of Mn did not readily occur at high current densities. The decrease in the discharge capacity and increase of ΔV at higher current rates was attributed to limitations of $LiMn_{0.8}Fe_{0.2}PO_4$ in meeting the demands of faster reaction kinetics at higher C-rates. This was due to intrinsic low electronic conductivity and slow lithium ion diffusion at the $LiMn_{0.8}Fe_{0.2}PO_4/Mn_{0.8}Fe_{0.2}PO_4$ solid interface.

The long-term cycle performance of the LMF5 solid battery up to 300 cycles at different C-rates is shown in Fig. 7b. Remarkably good long-term cycling properties were observed in the cathodes at all C-rates evaluated in this study at a high charge voltage of 4.5 V. After completion of 300 cycles, the discharge capacities realized at C-rates of 1, 3, and 10 were 129.86, 123.96, and 68.85 mAh g^{-1}, respectively. LMF5 showed >92% retention of its initial discharge capacity at the 300th cycle at a C-rate of 1. In addition, the cell performed equally well at C-rates of 3 and 10, retaining >97% of its initial discharge capacity at the 300th cycle. Of all the C-rates studied, the calculated capacity fade per cycle based on the initial discharge capacity of the cell and the following 300 charge-discharge cycles was very low (0.001–0.02%). Fig. S5 shows the penetration safety of the LMF5-based all-solid-state battery. Although the solid battery is punctured by a gun, it works safely without explosion. This render LMF5 and HSE with Al_2O_3 a very promising cathode and electrolyte material for high-voltage, all-solid-state batteries capable of safely delivering reliable performance at room temperature.

4. Conclusion

The effects of calcination temperature on the structural, morphological, and electrochemical properties of $LiMn_{0.8}Fe_{0.2}PO_4$ synthesized by a modified mechanical activation process were investigated for use as a cathode in high-performance all-solid-state batteries. Rietveld refinement analysis indicated the formation of pure-phase materials with changes in cell parameters caused by increasing calcination temperature. The length and angle of the Mn/Fe–O bond in Mn/Fe–O_6 octahedra changed with variations in synthesis temperature. The LMF5 had a crystal structure that allowed rapid lithium ion transfer. Scanning electron microscope analysis revealed a substantial increase in particle size with increasing calcination temperature above 500 °C. A relatively low reaction temperature of 500 °C produced well-crystallized, small particles with uniform sizes (60 nm) and morphologies. Lithium ions in LMF5 exhibited excellent charge-discharge kinetics. A LAGP-based hybrid solid electrolyte was prepared for use in a high voltage solid-state battery, and Al_2O_3 was added to the hybrid solid electrolyte to enhance the lithium ion transference number. Consequently, the lithium ion transference number was significantly improved to 0.81. The LMF5 solid battery material prepared at 500 °C in combination with the HSE exhibited initial discharge capacities of 156.3, 133.7, 111.8, and 71.4 mAh g^{-1} at C-rates of 0.1, 1, 3, and 10 C, respectively. Cycling at different current densities revealed the good performance capabilities of the LMF5-based solid battery, which had a low capacity fade even at the high current density of 10 C. $LiMn_{0.8}Fe_{0.2}PO_4$ active material and hybrid solid electrolyte with Al_2O_3 exhibiting reliable electrochemical performance in an all-solid-state battery at high charging voltages were realized by adopting the modified mechanical activation preparation process at an optimal synthesis temperature of 500 °C and incorporating a high dielectric constant ceramic in the hybrid solid electrolyte.

Credit author statement

Hakgyoon Yu: Writing.
Gil Chan Hwang: Reviewing and Editing.
Dong-Won Kang: Reviewing and Editing.

Declaration of Competing Interest

The authors declare no competing interests.

Credit authorship contribution statement

Hakgyoon Yu: Conceptualization, Investigation. **Jong Su Han:** Investigation. **Gil Chan Hwang:** Investigation. **Jung Sang Cho:** Investigation. **Dong-Won Kang:** Investigation. **Jae-Kwang Kim:** Conceptualization, Writing - review & editing, Supervision.

Acknowledgments

This research was supported by the Basic Science Research Program through the National Research Foundation of Korea (NRF), funded by the Ministry of Education (2017M1A2A2087577 and 2018R1A4A1024691).

Supplementary materials

Supplementary material associated with this article can be found, in the online version, at doi:10.1016/j.electacta.2020.137349.

References

[1] W.J. Zhang, Structure and performance of LiFePO[4] cathode materials: a review, J. Power Sources 196 (2011) 2962–2970.
[2] Z. Xu, L. Gao, Y. Liu, L. Li, Review—recent developments in the doped $LiFePO_4$ cathode materials for power lithium ion batteries, J. Electrochem. Soc. 163 (2016) A2600–A2610.

[3] X. Wang, Z. Feng, J. Huang, W. Deng, X. Li, H. Zhang, Z. Wen, Graphene-decorated carbon-coated $LiFePO_4$ nanospheres as a high-performance cathode material for lithium-ion batteries, Carbon N.Y. 127 (2018) 149–157.
[4] I. Seo, B. Senthilkumar, K.H. Kim, J.K. Kim, Y. Kim, J.H. Ahn, Atomic structural and electrochemical impact of Fe substitution on nano porous $LiMnPO_4$, J. Power Source 320 (2016) 59–67.
[5] K. Kim, J.K. Kim, Comparison of structural characteristics and electrochemical properties of $LiMPO_4$ (M=Fe, Mn, and Co) olivine compounds, Mater. Lett. 176 (2016) 244–247.
[6] Y. Maeyoshi, S. Miyamoto, Y. Noda, H. Munakata, K. Kanamura, Effect of organic additives on characteristics of carbon-coated $LiCoPO_4$ synthesized by hydrothermal method, J. Power Source 337 (2017) 92–99.
[7] D.B. Ravnsbæk, K. Xiang, W. Xing, O.J. Borkiewicz, K.M. Wiaderek, P. Gionet, K.W. Chapman, P.J. Chupas, M. Tang, Y.M. Chiang, Engineering the transformation strain in $LiMn_yFe_{1-y}PO_4$ olivines for ultrahigh rate battery cathodes, Nano Lett. 16 (2016) 2375–2380.
[8] Y. Wang, D. Zhao, R. Che, Y. Xia, Pseudo-capacitive profile vs. Li-intercalation in Nano-$LiFePO_4$, J. Power Sources 236 (2013) 230–237.
[9] Q. Li, F. Zheng, Y. Huang, X. Zhang, Q. Wu, D. Fu, J. Zhang, J. Yin, H. Wang, Surfactants assisted synthesis of nano-$LiFePO_4$/C composite as cathode materials for lithium-ion batteries, J. Mater. Chem. A 3 (2015) 2025–2035.
[10] G. Longoni, J. Kumar Panda, L. Gagliani, R. Brescia, L. Manna, F. Bonaccorso, V. Pellegrini, In situ $LiFePO_4$ nano-particles grown on few-layer graphene flakes as high power cathode nano hybrids for lithium-ion batteries, Nano Energy 51 (2018) 656–667.
[11] F. Yu, J. Zhang, Y. Yang, G. Song, Preparation and characterization of mesoporous $LiFePO_4$/C microsphere by spray drying assisted template method, J. Power Sources 189 (2009) 794–797.
[12] C. Torre-Gamarra, M.E. Sotomayor, J.-.Y. Sanchez, B. Levenfeld, A. Várez, B. Laïk, J.-.P. Pereira-Ramos, High mass loading additive-free $LiFePO_4$ cathodes with 500 μm thickness for high areal capacity Li-ion batteries, J. Power Sources 458 (2020) 228033.
[13] A. Kulka, A. Braun, T.W. Huang, A. Wolska, M.T. Klepka, A. Szewczyk, D. Baster, W. Zajac, K. Świerczek, J. Molenda, Evidence for Al doping in lithium sublattice of $LiFePO_4$, Solid State Ion. 270 (2015) 33–38.
[14] A. Eftekhari, $LiFePO_4$/C nanocomposites for lithium-ion batteries, J. Power Sources 458 (2017) 395–411.
[15] F. Croce, A.D. Epifanio, J. Hassoun, A. Deptula, T. Olczac, B. Scrosati, A novel concept for the synthesis of an improved $LiFePO_4$ lithium battery cathode, Eletrochem. Solid-State Lett. 5 (2002) A47–A50.
[16] A. Paolella, G. Bertoni, P. Hovington, Z. Feng, R. Flacau, M. Prato, M. Colombo, S. Marras, L. Manna, S. Turner, G. VanTendeloo, A. Guerfi, G.P. Demopoulos, K. Zaghi, Cation exchange mediated elimination of the Fe-antisites in the hydrothermal synthesis of $LiFePO_4$, Nano Energy 16 (2015) 256–267.
[17] P. Zhu, Z. Yang, H. Zhang, J. Yu, Z. Zhang, J. Cai, C. Li, Utilizing egg lecithin coating to improve the electrochemical performance of regenerated lithium iron phosphate, J. Alloys Compd. 745 (2018) 164–171.
[18] H.J. Kim, G.H. Bae, S.M. Lee, J.H. Ahn, J.K. Kim, Properties of lithium iron phosphate prepared by biomass-derived carbon coating for flexible lithium ion batteries, Electrochim. Acta 300 (2019) 18–25.
[19] C. Gong, Z. Xue, S. Wen, Y. Ye, X. Xie, Advanced carbon materials/olivine $LiFePO_4$ composites cathode for lithium ion batteries, J. Power Sources 318 (2016) 093–112.
[20] C. Delacourt, P. Poizot, M. Morcrette, J.M. Tarascon, C. Masquelier, A one step low-temperature route for the preparation of electrochemically active $LiMnPO_4$ powders, Chem. Mater. 16 (2004) 93–99.
[21] A. Yamada, M. Hosoya, S.C. Chung, Y. Kudo, K. Hinokuma, K.Y. Liu, Y. Nishi, Olivine-type cathodes: achievements and problems, J. Power Sources 232 (2003) 119–121.
[22] J.K. Kim, G. Cheruvally, H.J. Ahn, Electrochemical properties of $LiFePO_4$/C synthesized by mechanical activation using sucrose as carbon source, J. Solid State Electrochem. 12 (2008) 799–805.
[23] A. Yamada, S.C. Chung, K. Hinokuma, Optimized $LiFePO_4$ for lithium battery cathodes, J. Electrochem. Soc. 148 (2001) A224–A229.
[24] C. Delacourt, L. Laffont, R. Bouchet, C. Wurm, J.B. Leriche, M. Morcrette, J.M. Tarascon, C. Masquelier, Toward understanding of electrical limitations (Electronic, Ionic) in $LiMPO_4$ (M = Fe, Mn) electrode materials, J. Electrochem. Soc. 152 (2005) A913–A921.
[25] J. Ma, Q.Z. Qin, Electrochemical performance of nanocrystalline $LiMPO_4$ thin–films prepared by electrostatic spray deposition, J. Power Sources 148 (2005) 66–71.
[26] G. Li, H. Azuma, M. Tohda, Optimized $LiMn_yFe_{1-y}PO_4$ as the cathode for lithium batteries, J. Electrochem. Soc. 149 (2002) A743–A747.
[27] J.K. Kim, G. Cheruvally, J.W. Choi, J.U. Kim, J.H. Ahn, G.B. Cho, K.W. Kim, H.J. Ahn, Effect of mechanical activation process parameters on the properties of $LiFePO_4$ cathode material, J. Power Sources 166 (2007) 211–218.
[28] J.K. Kim, J.W. Choi, G. Cheruvally, J.U. Kim, J.H. Ahn, G.B. Cho, K.W. Kim, H.J. Ahn, A modified mechanical activation synthesis for carbon-coated $LiFePO_4$ cathode in lithium batteries, Mater. Lett. 61 (2007) 3822–3825.
[29] T. Drezen, N.H. Kwon, P. Bowen, I. Teerlinck, M. Isono, I. Exnar, Effect of particle size on $LiMnPO_4$ cathodes, J. Power Source 174 (2007) 949–953.
[30] A. Varzi, R. Raccichini, S. Passerini, B. Scrosati, Challenges and prospects of the role of solid electrolytes in the revitalization of lithium metal batteries, J. Mater. Chem. A 4 (2016) 17251–17259.
[31] M. Keller, A. Varzi, S. Passerini, Hybrid electrolytes for lithium metal batteries, J. Power Sources 392 (2018) 206–225.
[32] C. Liang, F. Kong, R.C. Longo, J.S.Kim S.KC, S.H. Jeon, S.A. Choi, K. Cho, Unraveling the origin of instability in Ni-rich $LiNi_{1-2x}Co_xMn_xO_2$ (NCM) cathode materials, J. Phys. Chem. C 120 (2016) 6383–6393.
[33] K. Qian, Y. Li, Y.B. He, D. Liu, Y. Zheng, D. Luo, B. Li, F. Kang, Abuse tolerance behavior of battery during overcharge and over-discharge, RSC Adv. 6 (2016) 76093–77104.
[34] J. Kalhoff, G.G. Eshetu, D. Bresser, S. Passerini, Safer electrolytes for lithium-ion batteries: state of the art and perspectives, ChemSusChem 8 (2015) 2154–2175.
[35] F. Zheng, M. Kotobuki, S. Song, M.O. Lai, L. Lu, Review on solid electrolytes for all-solid-state lithium-ion batteries, J. Power Sources 389 (2018) 198–213.
[36] Z. Gao, H. Sun, L. Fu, F. Ye, Y. Zhang, W. Luo, Y. Huang, Promises, challenges, and recent progress of inorganic solid-state electrolytes for all-solid-state lithium batteries, Adv. Mater. 30 (2018) 1705702.
[37] J.-.K. Kim, J. Scheers, T.J. Park, Y. Kim, Superior ion-conducting hybrid solid electrolyte for all- solid-state batteries, ChemSusChem 8 (2015) 636–641.
[38] Y.J. Lim, H.W. Kim, S.S. Lee, H.J. Kim, J.-.K. Kim, Y.-.G. Jung, Y. Kim, Ceramic-based composite solid electrolyte for lithium-ion batteries, Chempluschem 80 (2015) 1100–1103.
[39] J.-.K. Kim, Y.J. Lim, H. Kim, G.-.B. Cho, Y. Kim, A hybrid solid electrolyte for flexible solid-state sodium batteries, Energy Environ. Sci. 8 (2015) 3589–3596.
[40] http://www.ccp14.ac.uk/ccp/web-mirrors/fullprof/
[41] J.-.K. Kim, G. Cheruvally, J.-.H. Ahn, G.-.C. Hwang, J.B. Choi, Electrochemical properties of carbon-coated $LiFePO_4$ synthesized by a modified mechanical activation process, J. Phys. Chem. Solids 69 (2008) 2371–2377.
[42] K. Rissouli, K. Benkhouja, J.R. Ramos-Barrado, C. Julien, Electrical conductivity in lithium orthophosphates, Mater. Sci. Eng. B 98 (2003) 185–189.
[43] A. Yamada, Y. Takei, H. Koizumi, N. Sonoyama, R. Kanno, K. Itoh, M. Yonemura, T. Kamiyama, Electrochemical, magnetic, and structural investigation of the $Li_x(Mn_yFe_{1-y})PO_4$ olivine phases, Chem. Mater. 18 (2006) 804–813.
[44] M.S. Whittingham, Y. Song, S. Lutta, P.Y. Zavalij, N.A. Chernova, Some transition metal (oxy)phosphates and vanadium oxides for lithium batteries, J. Mater. Chem. 15 (2005) 3362–3379.
[45] D. Saikia, J.R. Deka, C.J. Chou, C.H. Lin, Y.C. Yang, H.M. Cao, Encapsulation of $LiFePO_4$ nanoparticles into 3D interpenetrating ordered mesoporous carbon as a high-performance cathode for lithium-ion batteries exceeding theoretical capacity, ACS Appl. Energy Mater. 2 (2019) 1121–1133.
[46] J.K. Kim, Y.J. Lim, H. Kim, G.B. Cho, Y. Kim, A hybrid solid electrolyte for flexible solid-state sodium batteries, Energy Environ. Sci. 8 (2015) 3589–3596.
[47] Y.J. Lim, H.W. Kim, S.S. Lee, H.J. Kim, J.K. Kim, Y.G. Jung, Y. Kim, Ceramic-based composite solid electrolyte for lithium-ion batteries, Chempluschem 80 (2015) 1100–1103.
[48] S.K. Chaurasia, R.K. Singh, S. Chandra, Ion-polymer complexation and ion-pair formation in a polymer electrolyte PEO:$LiPF_6$ containing an ionic liquid having same anion: a Raman study, Vib Spectrosc. 68 (2013) 190–195.
[49] J. Zhao, L. Wang, X. He, C. Wan, C. Jiang, Determination of lithium-ion transference numbers in $LiPF_6$–PC solutions based on electrochemical polarization and NMR measurements, J. Electrochem. Soc. 155 (2008) A292–A296.